WILEY | Hindawi

Research Article

Supersonically Sprayed Cobalt Titanate and PVDF for Flexible Piezoelectric Nanogenerators

Chanwoo Park [ID],[1] **Bhavana Joshi,**[1] **Edmund Samuel,**[2] **Byeong-yeop Kim,**[1] **Ali Aldalbahi** [ID],[3] **Mohamed El-Newehy,**[3] **Hae-Seok Lee** [ID],[2] **and Sam S. Yoon** [ID][1]

[1]*School of Mechanical Engineering, Korea University, Seoul 02841, Republic of Korea*
[2]*Energy Environment Policy and Technology, Graduate School of Energy and Environment (KU-KIST Green School), Korea University, Seoul 02841, Republic of Korea*
[3]*Department of Chemistry, College of Science, King Saud University, Riyadh 11451, Saudi Arabia*

Correspondence should be addressed to Hae-Seok Lee; lhseok@korea.ac.kr and Sam S. Yoon; skyoon@korea.ac.kr

Piezoelectric nanogenerators (PENGs) are the core components of self-powered devices used in sensors, ecofriendly wearable gadgets, and biomedical implants. This study introduces and demonstrates a flexible PENG with supersonically cold-sprayed films of cobalt titanate (CTO) and polyvinylidene fluoride (PVDF). An electrically poled PENG produces a maximum output voltage of 34.8 V under a tapping force of 20 N, whereas a CTO/PVDF-based PENG exhibits 25.4 V across a loading resistance (R_L) of 50 MΩ and generates a short-circuit current of 30 μA at 0.1 MΩ. Furthermore, the maximum power density is 25 μW·cm^{-2} at $R_L = 0.6$ MΩ. Cyclic tapping and bending test results show that open-circuit voltages (V_{oc}) of 25.4 and 5.8 V are produced under the tapping cycle of $N_{tap} = 4200$ and bending cycle of $N_{bend} = 750$, respectively, confirming the mechanical durability of the PENG. Thus, the potential of CTO/PVDF films for use in PENGs with various functionalities can be confirmed based on the V_{oc} values generated from bending, mobile tapping, walking, and lifting movements.

1. Introduction

Self-powered microelectronic devices, such as biomedical implants, portable electronics, and wireless sensors, require electrical energy, which can be converted from readily available ambient mechanical energy via piezoelectric nanogenerators (PENGs) [1–4]. PENGs harvest electrical energy using ambient mechanical energy to produce power in the range of microwatts to milliwatts [5–7], and this power is sufficient for use in microelectronic devices [8]. Moreover, small PENGs can power light-emitting diodes (LEDs) under tapping and bending conditions, indicating their usefulness in display applications [9]. PENG-based detection of human body movements is also gaining attention owing to emergence of wired or wireless human-machine interfaces and soft bioelectronics [10, 11]. Many of these applications require flexible and conformable components.

Flexible PENGs that use elastic polar organic polymers, resulting in a uniform distribution of the applied force, have been explored for pacemakers, artificial intelligence, and wearable electronics [12–14]. Polyacrylonitrile (PAN), poly L-lactic acid (PLLA), polyamide 11 (PA), polydimethylsiloxane (PDMS), and polyvinylidene fluoride (PVDF) are widely used to fabricate flexible PENGs [15]. The piezoelectric properties of PAN were first reported in 1984 [16]; however, PAN-based nonwoven fiber mats currently exhibit a piezopotential of only 6 V [17]. PLLA-based PENGs, which exhibit a moderate piezoelectric coefficient (3 pm/V), are used as bio-e-skin [18]. However, reports suggest that PLLA-based PENGs exhibit poor reproducibility, and their low output power poses a challenge [19, 20]. Thus, among the various polymer matrices, PVDF and its copolymers are more suitable piezopolymers for PENGs [21]. Various copolymers of PVDF (e.g., PVDF-co-hexafluoropropylene

(PVDF-HFP) and PVDF-trifluoroethylene (PVDF-TrFe)) have been thoroughly investigated, indicating that they are more useful as polar polymers for flexible PENGs. The main constituents of PVDF are nonpolar α- and polar β-phases, which provide mechanical stability and energy-harvesting capability, respectively [22, 23]. Although the α-phase is dominant in PVDF, various methods can transform it to yield β-phase-rich PVDF, which improves piezoelectric properties [21].

Enhancement of the electroactive phase of PVDF has been reported using various techniques, for example, electrospinning owing to a high electric field [24, 25], spin coating owing to the high-speed rotation of a viscous PVDF-based sol-gel [26], and cold spraying owing to shear stress and stretching due to the deposition of precursor droplets with supersonic velocity [9]. However, in each of these techniques, due to the absence of ceramics, the PVDF-based PENG experiences significant constraints, i.e., low piezopotential output caused by the insufficient transformation of the β-phase in PVDF [26]. Therefore, the PVDF matrix requires fillers to improve the piezoelectric performance of the PENG. Titanate-based piezoceramics such as $BaTiO_3$, $PbTiO_3$, and $PbZrTiO_3$ are used because of their high piezoelectric coefficients [6, 27]. They possess a higher dielectric constant than PVDF, which introduces a dielectric mismatch and requires a higher concentration of ceramic fillers.

In contrast, a smaller number of low dielectric constant fillers are appropriate for the PVDF matrix to fabricate PENGs [28]. Moreover, fillers with a high dielectric constant are more susceptible to electrical breakdown; hence, the use of fillers with a low dielectric constant in PVDF has attracted considerable attention from the research community [28, 29]. Recently, transition metal (M) titanates (where M = Fe, Mn, Ni, or Co) as fillers in PVDF have gained attention for improving PENG performance in terms of higher piezocurrent and power. These transition metals are beneficial for improving the conductivity of electrons generated during mechanical energy harvesting. Because the electrical conductivity of PVDF is poor, charge accumulation and electron transfer are limited; hence, fillers are required to enhance the piezopotential. Nevertheless, exceedingly high conductivity, which subsequently reduces the output power of the PENG device, is not suitable for developing potential at the extreme surface of piezomaterials. Therefore, to achieve a high PENG output power, the addition of transition metal-based oxides to a PVDF matrix as a filler is advantageous [30]. For example, cobalt can enhance the piezoelectric coefficient of piezocomposites; therefore, cobalt titanate (CTO) is a potential candidate for the filler of the PVDF matrix [31, 32]. Moreover, the presence of fillers in the PVDF/N,N-dimethylformamide (DMF) solution is beneficial to achieve β-phase-rich PVDF and a highly effective piezoelectric coefficient. To the best of our knowledge, the use of CTO-based flexible PENGs has not been reported.

Herein, we report the synthesis of cobalt titanate (CTO) using a wet chemical process, followed by air annealing at 600°C. The annealed CTO powder was then dispersed in PVDF/DMF to prepare a precursor solution for supersonic cold spraying. The supersonic cold-spraying technique is vac-

uum-free, fast, and scalable and can produce crystalline polymer phases owing to its supersonic speed, which can result in high stretching rates for polymer coatings [33, 34]. The supersonic air velocity in the cold spray drives the droplets that carry PVDF and CTO, and the viscous nature of PVDF and dispersed CTO results in shear forces during motion and deposition. The shear forces and stretching of PVDF in the presence of CTO rearrange PVDF at the macromolecular level, leading to phase transformation of PVDF, which improves the piezoelectric output [9, 35]. The CTO/PVDF concentration was optimized and tested under tapping and bending forces. In addition, electrical poling was performed to enhance the piezoelectric potential. Moreover, the capability of the CTO/PVDF-based PENG was demonstrated with biomechanical bending and tapping movements such as grasping (bending and compressive force impact), elbow bending, and keyboard typing.

2. Experiments

2.1. Materials.
Cobalt(II) acetate tetrahydrate ($Co(CH_3COO)_2 \cdot 4H_2O$, ACS reagent, ≥98%, Sigma-Aldrich, USA), titanium(IV) butoxide ($Ti(C_4H_9O)_4$, 99.999% trace metal basis, Sigma-Aldrich, USA), ethylene glycol (99%, DUKSAN, Republic of Korea), poly(vinylidene fluoride) (PVDF, average M_w ~ 534,000, Sigma-Aldrich, USA), deionized water (DI water, SAMCHUN, Republic of Korea), ethyl alcohol (ethanol, 99.9% GR grade, DUKSAN, Republic of Korea), and N,N-dimethylformamide (DMF; anhydrous, 99.8%, Sigma-Aldrich, USA) were used to synthesize CTO and CTO/PVDF composite films. Polyimide tape (thickness: 50 μm), Cu tape (thickness: 100 μm), and Cu foil (thickness: 100 μm) were used to fabricate the PENG.

2.2. Synthesis of CTO Particles and CTO/PVDF Precursor Solutions.
Cobalt titanate particles were prepared by mixing cobalt(II) acetate tetrahydrate, titanium(IV) butoxide, and ethylene glycol. Initially, 7.47 g cobalt(II) acetate tetrahydrate was added to 300 mL of ethylene glycol, and the solution was stirred (HSD-180 magnetic stirrer, Misung Scientific Co., Republic of Korea) at 500 rpm for 5 min. Then, 10.2 mL of titanium(IV) butoxide was added dropwise to the cobalt(II) acetate tetrahydrate solution with stirring at 500 rpm. The mixture was then stirred at 500 rpm for 2 h. The red-colored solution turned light pink, indicating the formation of a metal-glycolate polymer chain. The obtained precipitate was washed five times with DI water and ethanol in a centrifuge (Rotofix 32 A, Hettich, USA) at 4000 rpm for 5 min to remove impurities. The washed particles were kept on a hot plate at 90°C overnight for drying. Finally, the dried separated particles were heated at a ramp rate of 5°C/min and annealed at 600°C for 5 h, yielding green-colored crystalline CTO particles.

The CTO/PVDF precursor solutions were prepared by varying the concentration of CTO (0.05, 0.1, 0.2, and 0.3 g, referred to as CTO1, CTO2, CTO3, and CTO4, respectively) in PVDF/DMF for the deposited flexible composite films (Table 1). The PVDF/DMF solutions were prepared by adding 1 g of PVDF to 30 mL of DMF and stirring at 80°C and 500 rpm for 3 h. Subsequently, the CTO particles (0.05, 0.1,

TABLE 1: Concentrations of CTO, PVDF, and DMF for various flexible CTO/PVDF composite films.

Case	CTO (g)	PVDF (g)	DMF (mL)
CTO1	0.05	1	30
CTO2	0.10	1	30
CTO3	0.20	1	30
CTO4	0.30	1	30

0.2, and 0.3 g) were added to the PVDF/DMF solutions, yielding the four different CTO/PVDF precursor solutions.

2.3. CTO/PVDF Film Deposition. The supersonic cold-spraying process included an air compressor (Padc-50, Asea Tacs, Republic of Korea), air heater (F076250, Joowon heater, Republic of Korea), converging–diverging supersonic nozzle (de Laval nozzle), atomizer (VCX134, Sonics & Materials, Inc., USA), and syringe pump (Legato 210, KD Scientific Inc., USA) [36–38]. Figure 1(a) shows the cold-spraying process of the CTO/PVDF composite film onto a Cu foil mounted to the $X – Y$ stage. Various samples were deposited by maintaining an air temperature of 250°C and an air pressure of 2 bar using a compressor. The air passed through the nozzle and accelerated to supersonic velocity. The CTO/PVDF precursor solution was supplied at 1.5 mL/min (through a syringe pump) to an atomizer placed at the nozzle outlet to form aerosols. DMF was vaporized during the supersonic spraying of the CTO/PVDF precursor solution; therefore, only CTO/PVDF was deposited. The CTO/PVDF films were deposited using ten passes ($N = 10$) of the $X – Y$ stage. The operating conditions of the supersonic cold-spraying process are listed in Table 2.

2.4. Characterization. Field emission scanning electron microscopy (FE-SEM; 653 S-5000, Hitachi, Ltd., Japan) was used to observe the surface morphologies of the composite films. Atomic force microscopy (AFM, NX-10, Park Systems, USA) in the piezoresponse force microscopy (PFM) mode was used to obtain the converse piezoelectric effect in the samples by detecting variations in the PFM tip amplitude. These variations were used to calculate the effective piezoelectric coefficient (d_{33}^*) using the following equation [39]:

$$d_{33}^* = \frac{3 \times \text{PFM amplitude}}{\text{sensitivity} \times \text{DC gain}} \times \frac{1}{V_T}. \tag{1}$$

Here, "sensitivity" denotes the vertical sensitivity of the tip ($\sim 33 \times 10^6$ V·m^{-1}), the DC gain is 3.4, and V_T denotes the tip bias (AC) maintained at 1 V.

X-ray diffraction (XRD; SmartLab, Rigaku, Japan) was performed at 0.5°/min to determine the crystalline structures of the CTO and PVDF particles. Fourier transform infrared spectrometry (FTIR; Spectrum GX, PerkinElmer Inc., USA) was used to analyze the α- and β-phases of PVDF. The morphology and elemental mapping of the CTO2 composite film were acquired by transmission electron microscopy (TEM; JEM 2100F, JEOL, Inc., Japan) and energy dispersive X-ray spectroscopy (EDS), respectively. High-resolution TEM (HRTEM) and selected-area electron diffraction (SAED) were used to analyze the interatomic spacing of the CTO2 film. A focused ion beam (FIB; FEI Helios G4 UX, Thermo Fisher Scientific, USA) was used to prepare samples for TEM.

2.5. PENG Fabrication. The PENG was assembled as a layered structure. First, polyimide tape (PI), 6 cm × 6 cm, was used as an insulating backing layer, and a 5 cm × 5 cm copper foil as a current collector was attached to the PI. In addition, a Cu foil strip (0.5 cm × 6 cm) was cut and attached to the lower left corner of the copper foil to electrically connect the PENG to an oscilloscope. The CTO/PVDF film with dimensions of 3 cm × 3 cm was placed on top at the center of the copper foil. Subsequently, a polyimide tape strip (1 cm × 6 cm) was attached to the edges of the CTO/PVDF/ Cu foil to ensure insulation, and a copper tape (5 cm × 5 cm) current collector was attached to the top. Finally, a Cu foil strip (0.5 cm × 6 cm) was attached to the lower right corner of the top Cu current collector to connect it to the oscilloscope during PENG testing. For simplicity, the PENGs were fabricated using the CTO1, CTO2, CTO3, and CTO4 composite films, and the corresponding PENG devices are referred to by the same name during the discussion of PENG characteristics. The structures of the CTO-based PENGs under various testing conditions are shown in Figure 1(b). The inset snapshots and illustrations show the tapping and bending tests for the CTO-based PENG, respectively. Figure 1(c) shows how the flexible CTO-based PENG can be configured on the human body. A PENG tapping power test and the resulting lighting of LEDs by the PENG are also shown in Figure 1(c).

2.6. PENG Device Property Measurement Details. The PENGs made from CTO/PVDF-based films deposited using the supersonic cold-spraying technique were subjected to various tapping forces (1, 5, 10, 15, and 20 N) and frequencies (1, 3, 5, and 7 Hz) using a tapping machine (SnM, Republic of Korea). The bending tests (Ocean Science Co., Ltd., 722, Republic of Korea) were performed at different bending radii ($R_b = 1, 2, 3, 4,$ and 5 mm) and bending rates (0.1, 0.5, 1, and 1.25 Hz). Electrical poling was performed using a high-voltage supply (Glassman High Voltage, Inc., USA). An electric field was applied to the PENG sample at 100 kV/cm (according to the PENG sample thickness) and maintained for 5, 10, or 15 h. The open-circuit voltages (V_{oc}) and output voltages across the load (V) of the polarized CTO-based PENG samples were measured using an oscilloscope (DS1052E RIGOL, China). To calculate the current (I) and power (P) of the CTO-based PENG, the output V was measured while changing the resistance (R) from 0.1 to 50 MΩ. Current and power were calculated using the following equations, respectively, based on the measured V.

$$I = \frac{V}{R}, \tag{2}$$

$$P = \frac{V^2}{R}. \tag{3}$$

(a) Supersonic deposition

(b) PENG structure and fabrication
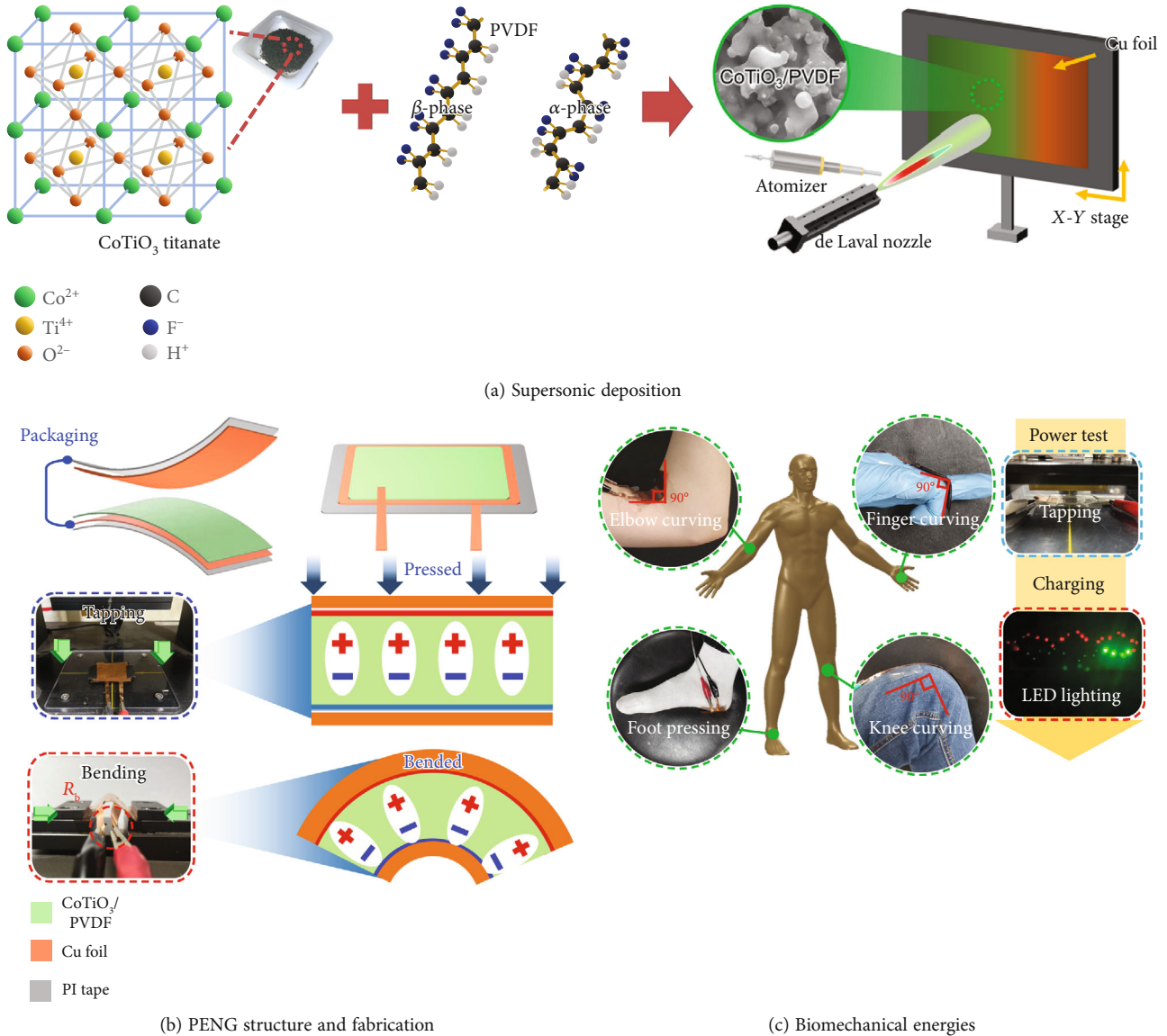

(c) Biomechanical energies

FIGURE 1: (a) Supersonic cold spraying of cobalt titanate powder and PVDF for the CTO/PVDF film. (b) Structure and fabrication of CTO-based PENGs under various tests. (c) Biomechanical piezopotential generation: bending CTO-based PENGs attached to different body parts, tapping PENG, and lighting red and green LED using the generated piezopotential.

TABLE 2: Operating conditions of the cold-spray device during deposition.

Cold-spraying parameter	Values
Pressure (bar)	2.0
Heater temperature (°C)	250.0
Solution flowrate (mL/min)	1.5
Traverse speed (mm/s)	15.0
Spraying distance (cm)	18.0
Number of passes	10.0

3. Results and Discussion

3.1. Characterization of CTO/PVDF Films. A CTO/PVDF composite film requires that the CTO particles are optimally incorporated within the PVDF matrix to achieve excellent piezoelectric performance. Therefore, the morphologies of the films were analyzed using SEM (Figure 2). The brighter spots encircled in the SEM images indicate the presence of CTO particles (Figure 2(a)). The darker regions in most places and around the brighter spots suggested the presence of a PVDF matrix (Figure 2(b)). SEM images of CTO1 are shown in Figure 2(a), indicating that the CTO particles were completely immersed in the PVDF matrix owing to their lower concentration in the precursor solution. The low-magnification SEM image revealed that the CTO particles were well dispersed; however, their concentration was lower in a given unit area. Upon increasing the CTO concentration in CTO2, numerous particles were well dispersed. The increase in the number of particles without agglomeration suggests that the PVDF matrix in the CTO2-based PENG
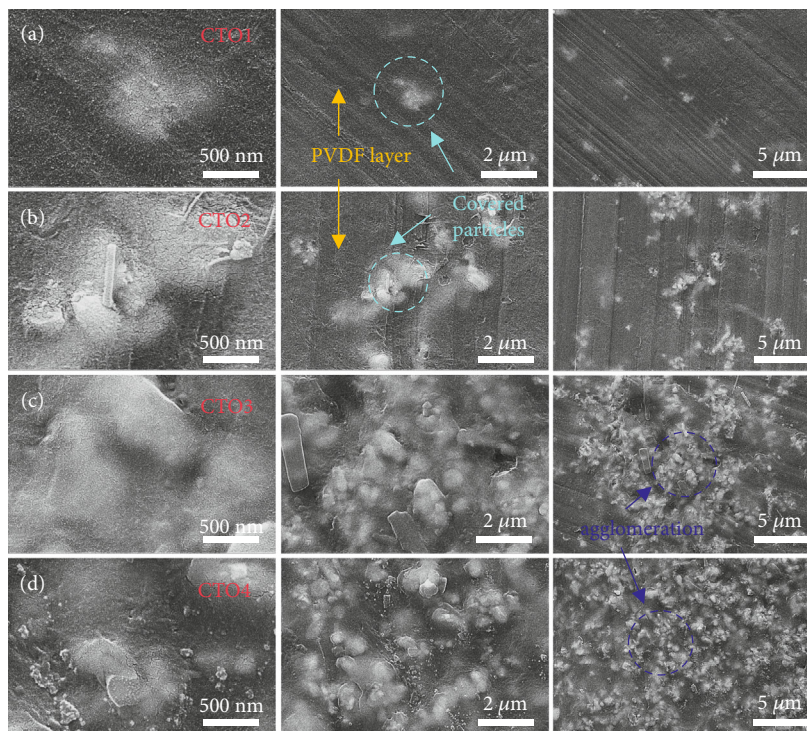
FIGURE 2: SEM images of CTO/PVDF composite films at three different magnifications: (a) CTO1, (b) CTO2, (c) CTO3, and (d) CTO4.

can improve the strain-induced polarization better than that in the CTO1-based PENG. However, with a further increase in the number of particles in CTO3 and CTO4, the composite films exhibited agglomeration and CTO particles were exposed (Figures 2(c) and 2(d)), owing to the relatively high ratio of CTO to PVDF (Table 1). Agglomerated CTO particles were visible in the low-magnification SEM images of CTO3 and CTO4 (Figures 2(c) and 2(d)). Such agglomerated particles and inconsistent PVDF matrices in composite films are not favorable for harvesting energy from ambient mechanical forces [40–42].

The structural properties of the CTO powder were analyzed by XRD, as shown in Figure S1. The Rietveld refinement of CTO powder was carried out by material analysis using diffraction (MAUD) software for five iterations, and the result was 68% $CoTiO_3$ and 32% of TiO_2 (Figure S2). The diffraction peaks of $CoTiO_3$ at 23.9, 32.7, 40.4, 48.9, 53.5, 56.8, 61.9, 63.5, 68.8, 70.9, and 75.1° corresponded to the (012), (104), (113), (024), (116), (018), (124), (300), (208), (1010), and (220) planes, respectively. The diffraction peaks of anatase TiO_2 at 25.2°, 37.8°, 47.9°, 55°, 62.6°, and 70.2° correspond to the (101), (004), (200), (211), (204), and (220) planes, respectively. The diffraction patterns of $CoTiO_3$ and anatase TiO_2 matched well with JCPDS No. 77-1373 and 21-1272, respectively. The XRD results for CTO1, CTO2, CTO3, CTO4, and the powders are provided in Figure S1 (also see Table 1). The intensity of the CTO peaks increased proportionally with CTO concentration, and the highest peak intensity was observed for CTO4. In all cases, the main peaks of PVDF were observed at $2\theta = 18.4°$ and 19.36°, corresponding to the (020) and (110) planes, respectively (JCPDS 38-1638) [43].

However, the peak was widened at around $2\theta = 20.2°$, owing to the appearance of the β-phase.

Cold spraying of the CTO/PVDF solution at supersonic velocity caused a shear force on the PVDF/DMF solution, and subsequent stretching occurred during flight. In addition, supersonic flow causes a catastrophic impact when the droplets hit the substrate. These effects (shear force and catastrophic impact) further escalate in the presence of CTO particles, resulting in the enhancement in the transformation of α-phase to β-phase of PVDF. Figure 3(a) depicts the cold-spraying scenarios of low and high concentrations of CTO particles. When the amount of CTO particles in the PVDF/DMF solution is lower, the folded chain (α-phase) of PVDF experiences turbulence while interacting with CTO particles. As a result of the shear forces on PVDF that occur due to the particle-polymer interaction, the CTO particles (scenario 1) unfold the folded chains of PVDF, i.e., transformation of the α-phase to the β-phase of PVDF. However, excess amount of CTO particles (scenario 3) restricts movement of PVDF, and there is less beneficial interaction between CTO and PVDF, which reduces the α-phase to β-phase transformation process. Thus, the optimal amount of CTO particles (scenario 2) is required to maintain the shearing interaction between CTO and PVDF and to achieve a greater orientation of the polar β-phase, which results in superior piezoelectric characteristics. In addition, the polar segment of PVDF adheres to the CTO particle during precursor solution processing or cold spraying, forming a heterostructure interface, and subsequently causes spontaneous polarization. This polarization is known as heterostructure interface polarization (HIP), as indicated in Figure 3(a). In contrast, the interface between
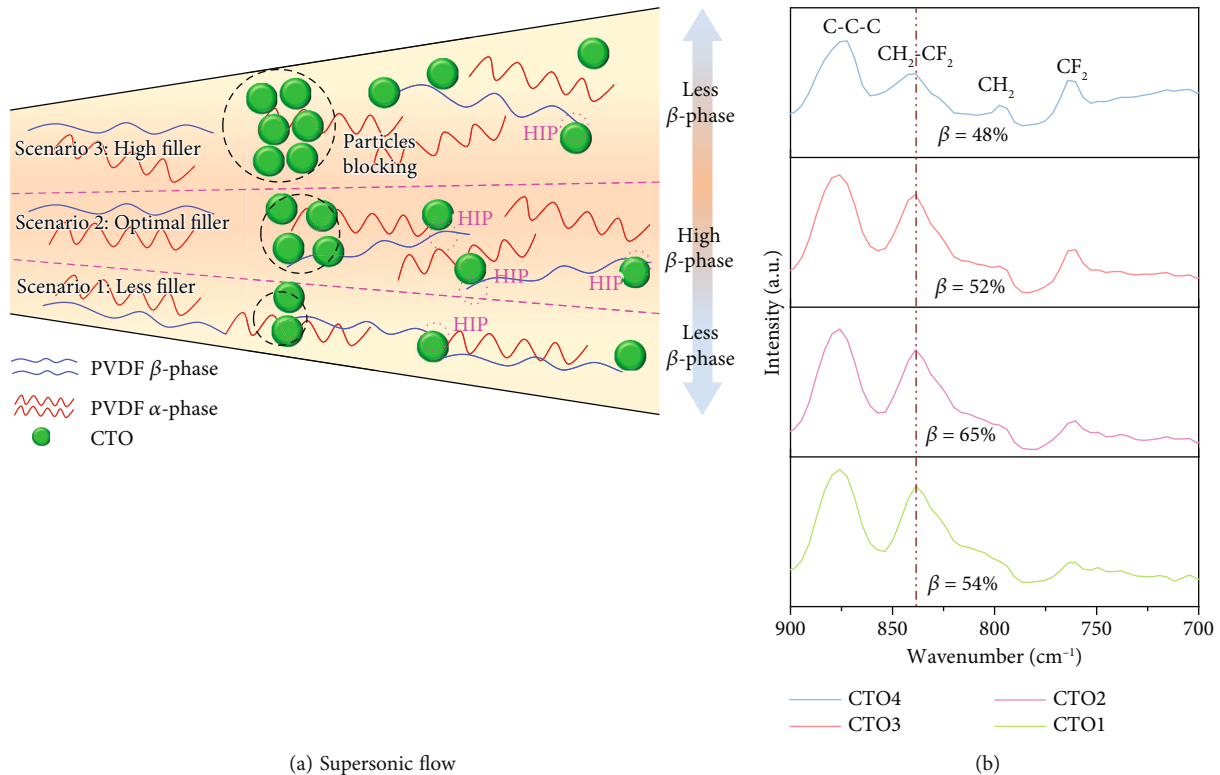
(a) Supersonic flow

(b)

FIGURE 3: (a) Effect of supersonic velocity and CTO particle concentration on crystalline phases of PVDF and (b) FTIR for CTO/PVDF samples.

CTO and the nonpolar segment of PVDF did not result in the formation of HIP. The CTO/PVDF heterostructure, as confirmed by the SEM images, results in the even distribution of CTO particles in the PVDF matrix. Cold spraying of colloidal CTO and the PVDF/DMF precursor solution resulted in a flexible heterostructured CTO/PVDF film owing to mutual adhesion at the interfacial sites [44].

Figure 3(b) compares the FTIR spectra in absorbance mode of the CTO/PVDF sample. The FTIR spectra exhibited peaks at $840\,cm^{-1}$, which was attributed to CH_2-CF_2 asymmetric stretching of the β-phase in PVDF. The peaks at 763, 795, and $872\,cm^{-1}$ correspond to CF_2 bending, CH_2 rocking, and C-C-C stretching of the α-phase of PVDF. The α-phase of the CTO1 and CTO2 samples is less than that of PVDF powder. By contrast, the β-phase fraction of CTO1 and CTO2 was observed to be 54 and 65%, respectively [9]. This increase in the β-phase fraction is beneficial to increase the interfacial sites between PVDF and CTO particles [45]. However, a higher amount of CTO in PVDF reduced the β-phase to 52 and 48% in the case of CTO3 and CTO4. As shown in scenario 3 of Figure 3(a), excess amounts of CTO particles inhibit the PVDF passage and ultimately reduce the interfacial interaction between CTO and PVDF, thus decreasing the β-phase transformation.

Piezoelectric force microscopy (PFM) was used to determine the effective piezoelectric coefficients of the composite films. The d_{33}^* values of the composite films were acquired by applying an electric field, which resulted in the deformation of the samples, and the mechanical strain on the composite

film generated a charge. This phenomenon is referred to as the converse piezoelectric effect [46]. Figures 4(a)–4(d) show the charge distribution profiles of the composite films. The deviation in the PFM tip amplitude was represented by the variation in the developed charge. The average amplitude values were 10.7, 15, 3.2, and 2.4 mV for CTO1–CTO4, respectively. In the case of CTO1, the concentration of the CTO particles was lower; hence, the charge distribution profile in Figure 4(a) appeared to be much smoother than in the other cases. As the amount of CTO particles increased to 0.1 g in the composite film, the charge distribution profile exhibited a greater shift in the amplitude of the PFM tip; hence, the average amplitude increased to 15 mV (Figure 4(b)). Because the CTO concentration was higher in CTO2 than in CTO1, the intergranular stress introduced relatively more polarization at the interface between the PVDF and CTO particles. However, with a further increase in CTO concentration in the composite films, the relative amount of PVDF was reduced, resulting in a very thin coating on the CTO particles; therefore, the average amplitude values were reduced to 3.2 and 2.4 mV for CTO3 and CTO4, as shown in Figures 4(c) and 4(d), respectively. In the case of CTO4, along with the thin PVDF coating, the CTO particles appeared to agglomerate, decreasing the effect of the applied field and mechanical deformation. Thin PVDF coatings and agglomeration issues are observed in the SEM images (Figures 2(c) and 2(d)). Accordingly, using the average amplitudes of the respective cases and Equation (1), the d_{33}^* values were estimated to be 286, 401, 85, and $64\,pm\cdot V^{-1}$ for the CTO1, CTO2, CTO3, and CTO4
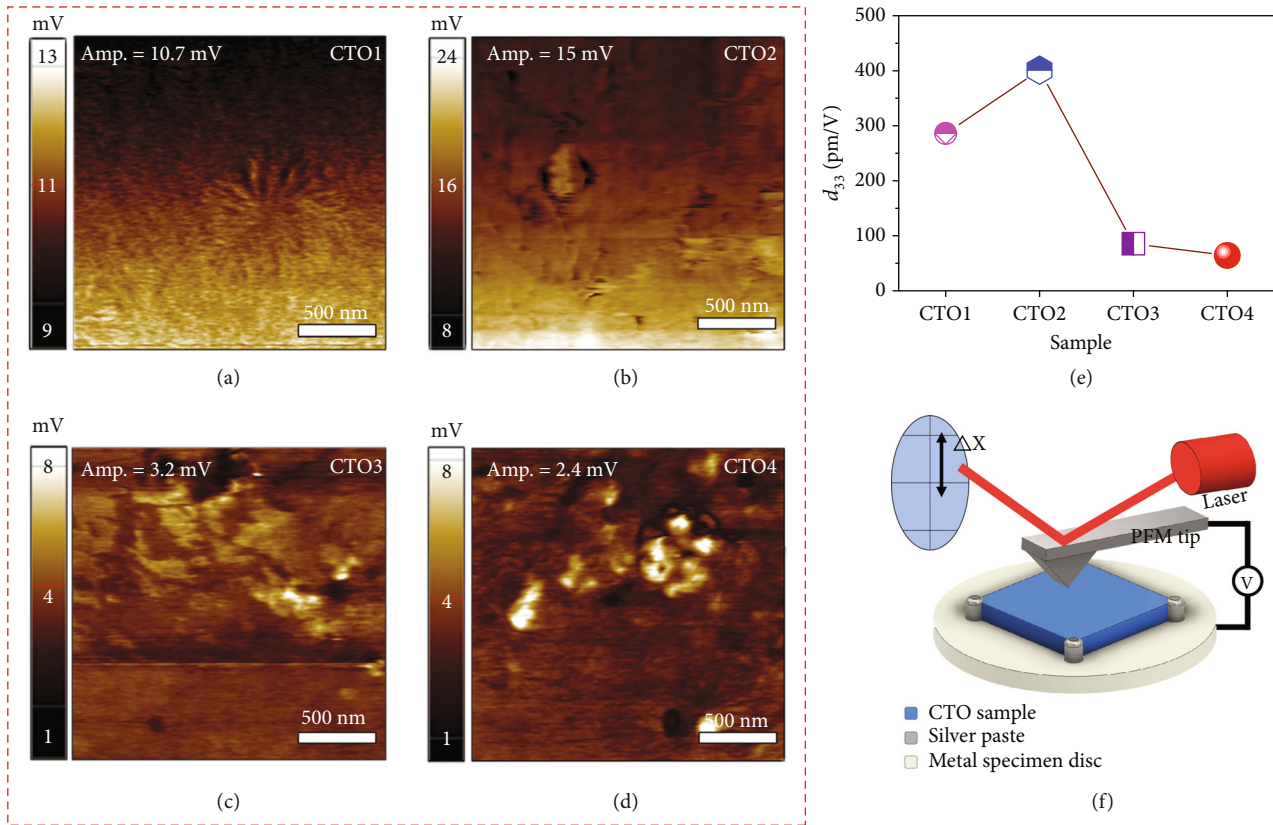
FIGURE 4: PFM amplitudes of (a) CTO1, (b) CTO2, (c) CTO3, and (d) CTO4. (e) Effective piezoelectric coefficient (d_{33}^{*}) of the composite films. (f) PFM measurement system.

composite films, respectively, which are graphically represented in Figure 4(e) [47]. In contrast, the d_{33}^{*} value of PVDF and CTO was estimated to be 43 and 2.35 pm·V^{-1}. Thus, it is evident that the d_{33}^{*} value of PVDF is enhanced owing to the addition of CTO that increases the electroactive β-phase of PVDF in the composite. A simple schematic of the converse piezoelectric effect measurement using PFM is shown in Figure 4(f). The shift in the PFM tip was detected using the laser sensor and indicated by Δx corresponding to the change in the charge on the surface of the composite films (CTO samples).

Figure 5(a) shows the TEM image of the FIB-milled CTO/PVDF film. A high-magnification image of a CTO particle, marked with a red circle, is shown in the inset of Figure 5(a). The HRTEM images in Figures 5(b) and 5(c) are well-resolved images obtained using GATAN (GMS 3, GATAN, USA). The HRTEM images shown in Figures 5(b) and 5(c) were captured from the blue-circle-marked site in Figure 5(a). The lattice spacing values of 0.27 and 0.25 nm corresponded to the (310) and (222) planes, respectively, which are consistent with the XRD data of CTO shown in Figure S1. In Figure 5(d), the SAED pattern exhibits diffraction spots, forming a ring with a lattice spacing consistent with the (310) and (440) CTO planes. The HRTEM and SAED results were consistent with the XRD data (Figure S1), confirming the presence of CTO. A high-magnification TEM image of the CTO particles (Figure 5(e)) was used for EDS mapping analysis.

The CTO particles exhibited a thin layer around them, which was attributed to the PVDF and formed a dielectric-semiconducting interface. The elemental maps of Co, Ti, O, and F are shown in Figures 5(f)–5(i). The appearance of Co, Ti, and O, consistent with the round particle, confirms the presence of CTO. In contrast, C and F from PVDF were observed to cover the CTO particles, which is essential for enhancing the piezoelectric performance.

3.2. Performance of the CTO-Based PENGs.
The PVDF-only-based PENG exhibited an output voltage of 8 V (Figure S3), owing to the electroactive phase of PVDF and piezoelectric characteristics, which led to the formation of dipoles during the tapping test [48, 49]. The V_{oc} values of CTO1, CTO2, CTO3, and CTO4 PENGs are shown in Figure 6(a). Adding CTO to PVDF increased the piezopotential to 14 and 21.6 V in CTO1 and CTO2, respectively. The piezopotential in the CTO/PVDF-based PENG was enhanced by the establishment of the Maxwell-Wagner-Sillars (MWS) polarization [50]. The MWS polarization is observed when the dielectric material is composed of semiconducting particles, which may develop capacitance in the case of the CTO/PVDF interface [30]. Free carriers of semiconducting particles such as CTO are blocked at the interface of the CTO/PVDF heterostructure due to different conductivities and permittivities, resulting in induced dipoles [51, 52]. This increase in polarization owing to the presence of fillers (CTO) resulted in an
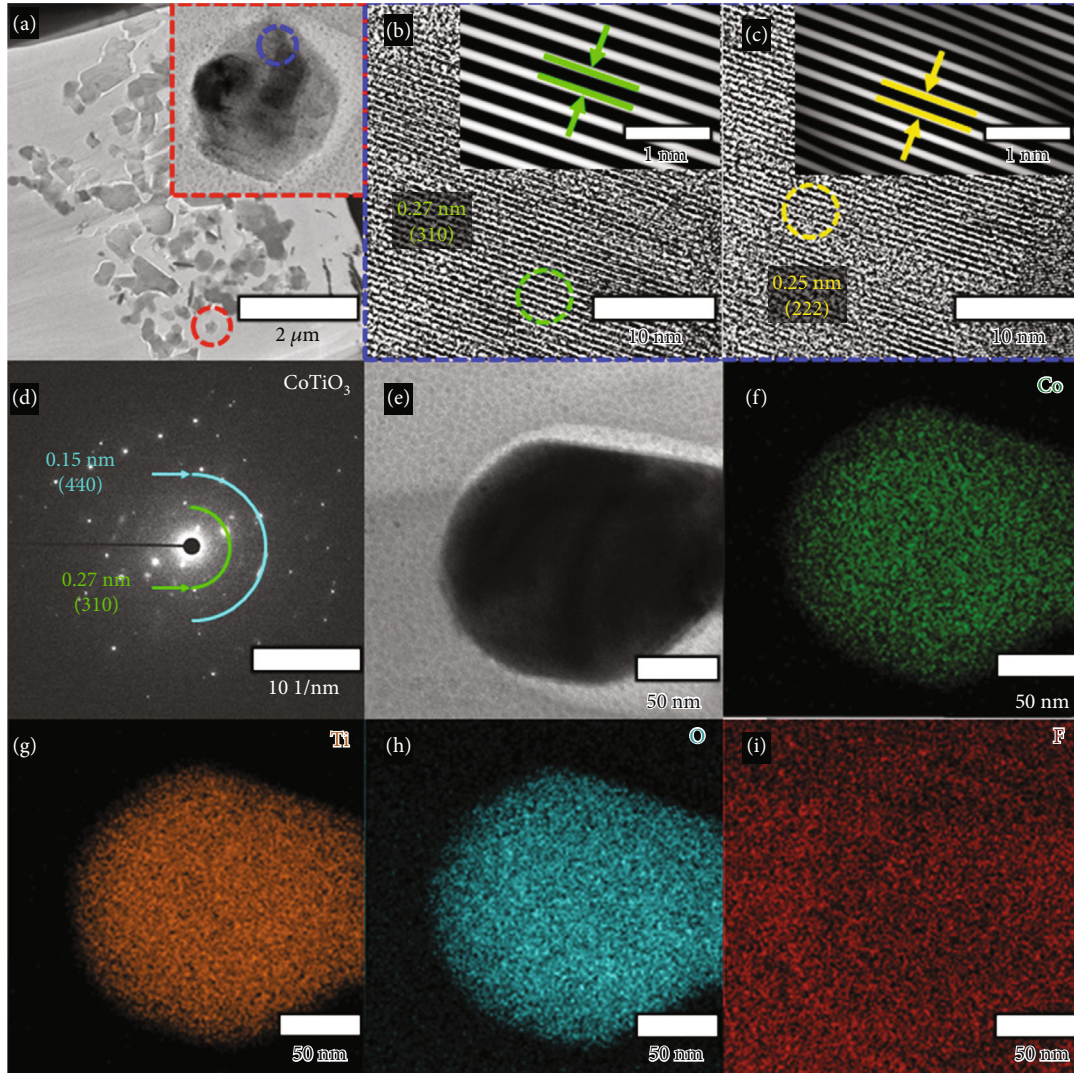
FIGURE 5: TEM images of CTO/PVDF: (a) morphology of the FIB-milled sample and (inset) a high-magnification image of a CTO particle, marked with a red circle; (b, c) high-resolution TEM images of the blue-circled area in (a); (d) selected area electron diffraction (SAED) pattern of CTO/PVDF; (e) TEM image of CTO particles surrounded by PVDF; (f–i) elemental mapping images of Co, Ti, O, and F.

increased piezopotential of the PENG, thereby improving its performance compared to that of pure PVDF (see Figure 6(a) and Figure S3). Surprisingly, CTO2 exhibited a low negative potential, the magnitude of which was less than that of CTO1 and CTO3. The low negative potential may be related to the optimal distance between the CTO particles, resulting in rapid neutralization of the electrode when the force is removed. However, with an increase in CTO content in CTO3 and CTO4, the potentials decreased to 13 and 10 V, respectively. This decrease in potential was caused by the reduction in the distance between the filler particles, which weakened the PVDF insulation, thereby compromising interfacial polarization. The SEM images (Figures 2(c) and 2(d)) show enhanced agglomeration and protruding CTO particles on the film surface, which facilitated higher charge migration and reduced the blocking of interfacial charges. The CTO2-based PENG with 0.1 g of CTO in 1 g of PVDF exhibited the optimal ratio, generating the highest piezopotential of 21.6 V at an

applied force of 20 N and a frequency of 5 Hz. The superior performance of CTO2 compared to the other samples (with lower or higher amounts of CTO) can be attributed to the enhanced interfacial sites between the CTO particles and the polar fraction of PVDF. The increased interface area subsequently promoted HIP formation, as shown schematically in Figure 3(a). The enhancement of charge accumulation owing to the larger HIP in the case of CTO2 compared to the other cases was also confirmed by the reverse piezoelectric effect determined using PFM. Thus, this performance was consistent with a relatively higher d_{33}^* value of 400 pm·V^{-1} for CTO2 (Figure 4(e)).

Furthermore, the tapping force and frequency affected the piezopotential (Figures 6(b) and 6(c)). As the tapping force increased from 1 to 20 N, V_{oc} increased from 7 to 21.6 V for CTO2 at 5 Hz. Similarly, with an increase in the tapping frequency from 1 to 7 Hz at 20 N, V_{oc} increased from 3.5 to 25.4 V, leading to a maximum potential of 25.4 V. This increase is linear and indicates the excellent
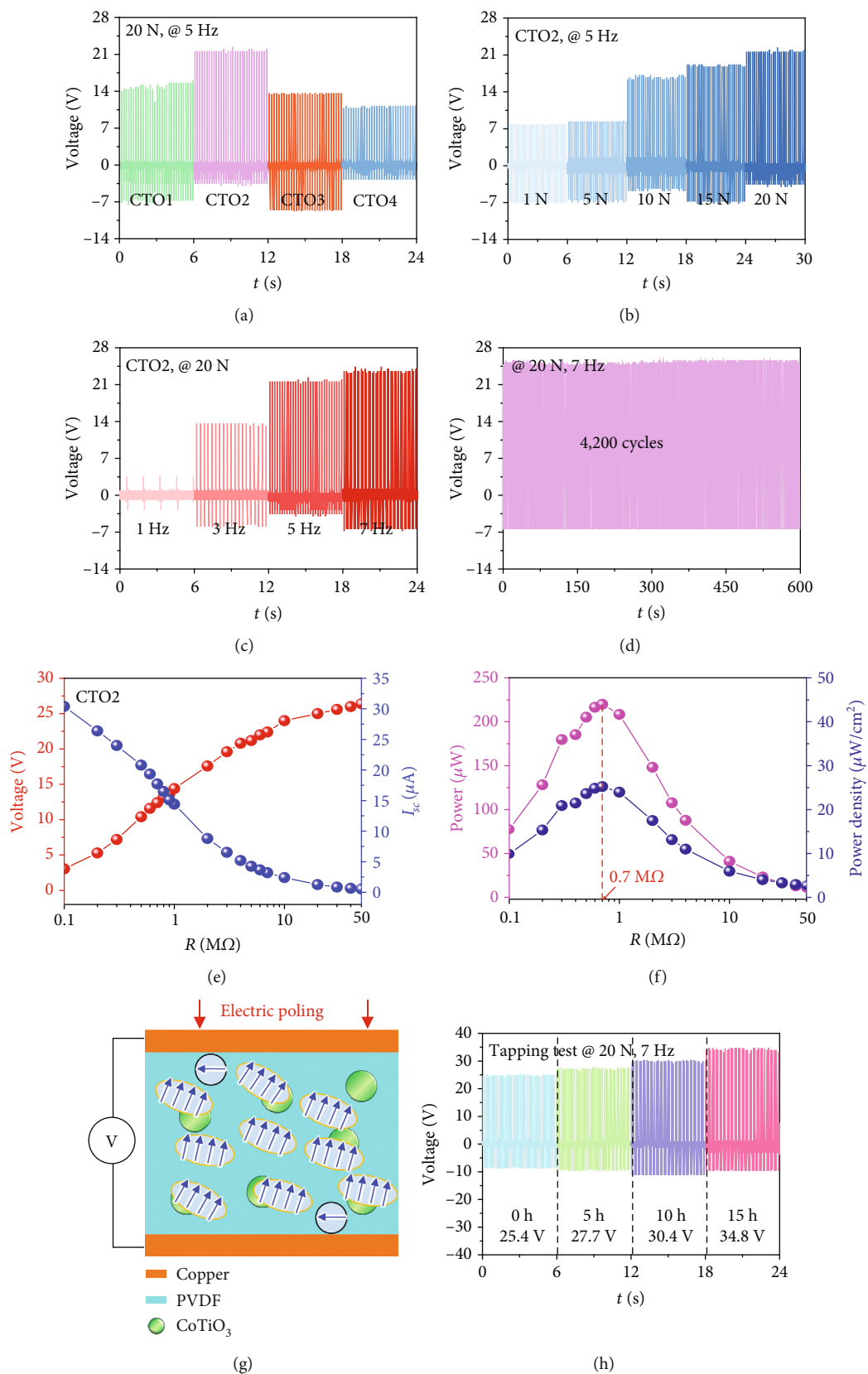
(a)

(b)

(c)

(d)

(e)
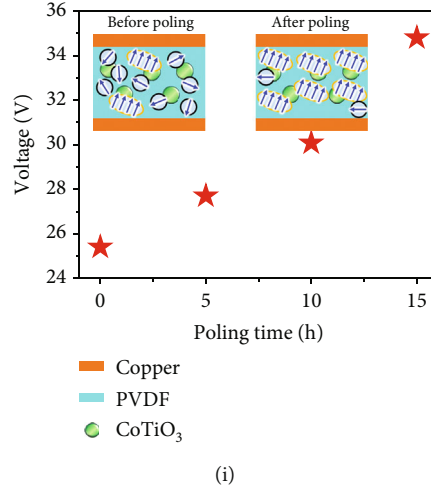
(f)

(g)

(h)

Figure 6: Continued.

(i)

FIGURE 6: Tapping test-generated V_{oc}: (a) effect of change in the concentrations of CTO from CTO1 to CTO4 at 20 N and 5 Hz; (b) effect of varying force on CTO2 at 5 Hz; (c) effect of frequency on CTO2 at 20 N; (d) 4200-cycle long-term tapping of CTO2-based PENG. (e, f) Variation in output voltage, current, power, and power density across load resistance. (g) Electrical poling of CTO2-based PENG circuit for the application of the electric field. (h) V_{oc} generated based on time-dependent electrical poling. (i) Increase in V_{oc} with poling (the inset depicts unaligned and aligned dipoles with interfacial polarization).

piezoelectric response of the PENG owing to the enhancement of the induced dipoles caused by the MWS polarization. Moreover, a greater imparting force or a faster force application rate increased the interfacial charge accumulation and improved the piezopotential [53]. The durability of the PENG under the application of a cyclic force was monitored using a long-term test conducted at 20 N and 7 Hz for 4200 cycles lasting for 600 s (Figure 6(d)). The PENG consistently exhibited a piezopotential of 25.4 V, without any decline, indicating excellent stability of the CTO/PVDF film (CTO2) as a PENG.

The working mechanism of the device and the necessity of a filler in the polymer matrix are schematically presented in Figure S4. PENG devices generate charges during harvesting of mechanical energy, and these charges accumulate at the extreme surfaces of the PENG material. Thus, upon application of mechanical forces, the accumulated charges cause the flow of electrons through an external circuit. Due to the piezoelectric/ferroelectric nature of PVDF and the presence of CTO particles, the electric dipoles were randomly oriented when no external force was applied; therefore, the net dipole moment was zero, and no piezoelectric potential appeared (Figure S4). When a small external force was applied, the PENG experienced strain and a small piezopotential was generated, as shown in Figure 6(b). An increase in the applied compressive force resulted in a larger piezopotential owing to the greater amount of strain. The presence of the CTO particles can amplify the strain, as shown in Figure 6(a). However, with an exceedingly large number of CTO particles, the compressive force was not sufficient to distribute the strain effectively to the PVDF and generated a lower piezopotential. Once the force was released, the accumulated charges moved in opposite directions, and a negative piezoelectric potential appeared (Figures 6(a)–6(d)). Therefore, the application and release of force resulted in an alternating piezocurrent (AC).

To determine the suitability of the PENG as a power source for self-powered devices, output voltage, current, and power were measured across a load resistance (R_L). The output voltage of the CTO2-based PENG at 50 MΩ is 25.4 V. The short-circuit current calculated from Equation (2) at 0.1 MΩ was 30 μA, which became zero with an increase in the load resistance (Figure 6(e)). These experimentally obtained current values were used to determine the theoretical capacitance of the PENG device using the following equation [54]:

$$I_{max} = \frac{d_{33} \cdot F}{C_{peng}(R + R_0)}, \tag{4}$$

where d_{33} is the piezoelectric coefficient obtained from PFM, F is the applied force, and R is the resistance. R_0 and C_{peng} are the internal resistance and capacitance of the PENG, respectively. To evaluate C_{peng}, the roots (or zeros) of the real-valued function Equation (4) were obtained using the Newton–Raphson method: R_0 was assumed comparable to the applied load resistance, whereas the computed C_{peng} varied until an error tolerance of <0.00001 was achieved. The obtained theoretical current values fit well with the experimentally obtained short-circuit currents (Figure S5a). The theoretical capacitance (C_{peng}) values decreased (see Figure S5b) with increasing load resistance, which could be attributed to the lower charge-transfer capability, causing less charge accumulation. The instantaneous power calculated using Equation (3) was 224 μW at 0.6 MΩ. The power density calculated based on the PENG's active area, i.e., 9 cm^2 (3 cm × 3 cm), was 25 μW·cm^{-2} at 0.6 MΩ (Figure 6(f)). The performance of the CTO2-based PENG was observed to be better compared to those of titanate-based PVDF composites, e.g., BaTiO$_3$/PVDF (0.8 μW·cm^{-2}) [55] and CaTiO$_3$/PVDF (0.19 μW·cm^{-2}) [56].
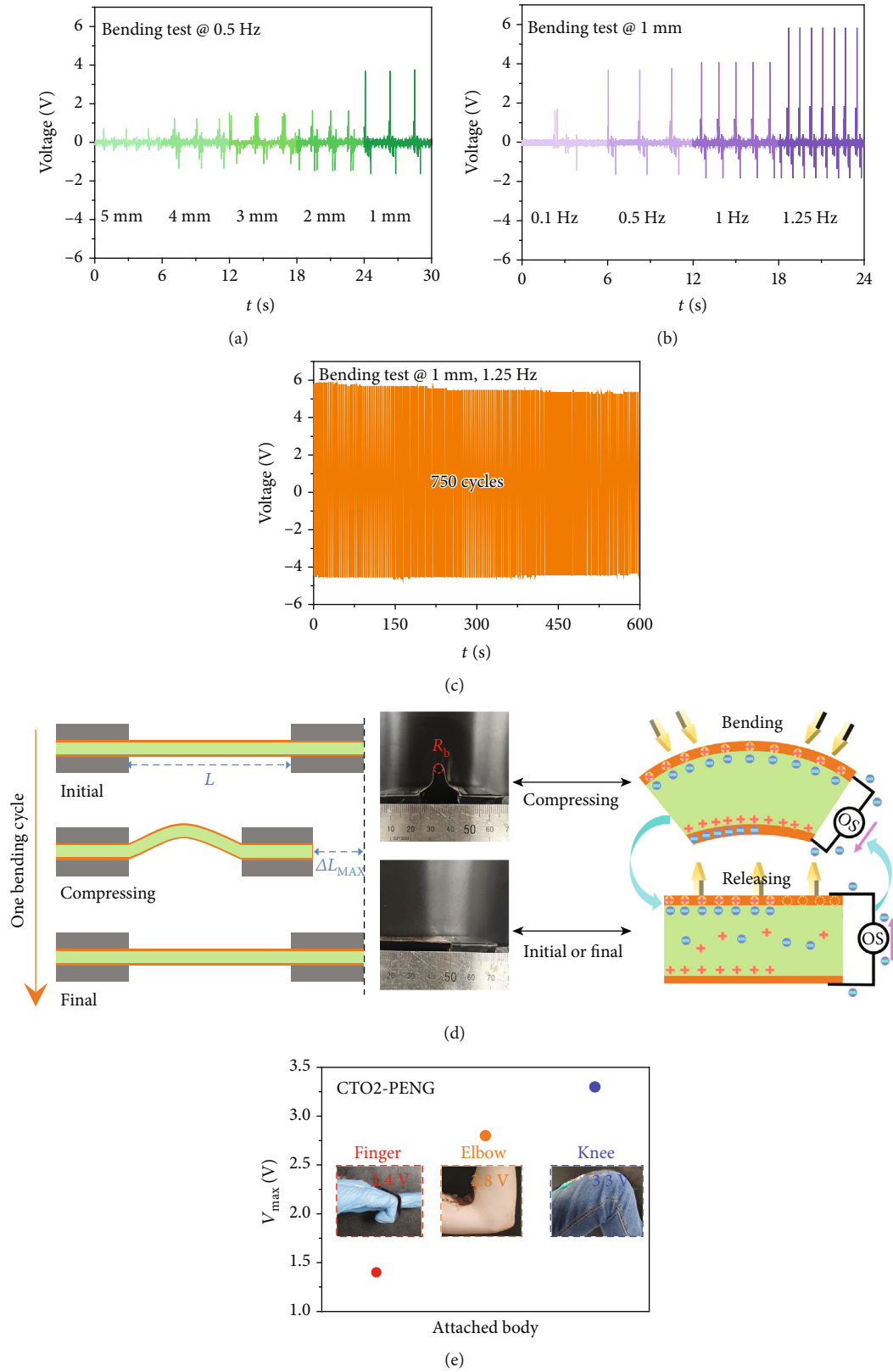
(a)

(b)

(c)

(d)

(e)

FIGURE 7: Voltage generated during bending: (a) V_{oc} of the bending test at different bending radii (R_b); (b) effect of bending frequencies for R_b of 1 mm; (c) long-term cycling for CTO2-based PENG; (d) mechanism under flat and bent conditions of the sample; (e) piezopotential generated by the PENG when attached to the finger, elbow, and knee, all bent at an angle of 90° (the inset images show the PENG attached to the body parts in the bent state).
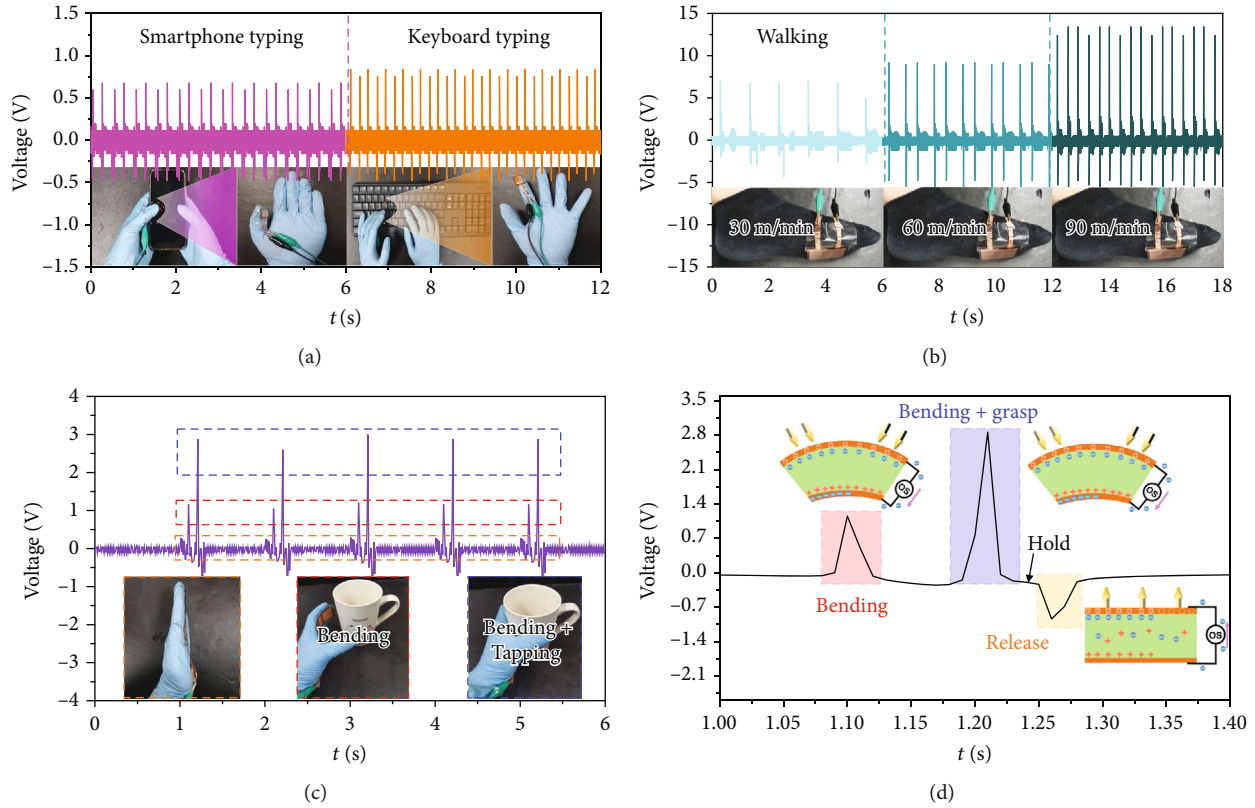
(a)

(b)

(c)

(d)

FIGURE 8: PENG application testing: (a) PENG attached to the finger while typing on a smartphone and keyboard; (b) PENG attached to the front foot while walking at different speeds; (c) PENG attached to the palm, with effect on piezopotential of the force generated during bending, grasping, and holding; (d) voltage vs. time curve depicting different states, confirming the suitability of the PENG for a tactile sensor.

The performance of piezoelectric materials is limited by their randomly oriented dipoles. Under mechanical stress, the dipoles rotate and align in the direction of the mechanical force. However, with a random orientation, the net polarization can be reduced, thereby generating a smaller piezopotential. The performance of piezoelectric materials can be improved by aligning the dipoles in the direction of a field. Applying an electric field of 100 kV/cm across the sample thickness (0.3 mm) induces a dipole alignment in the longitudinal direction, which is known as electrical poling. These prealigned dipoles reduce the energy required for the dipole rotation and enhance the net polarization and piezopotential. The degree of dipole alignment depends on the applied electric field strength and duration. Poling was performed for various durations using an electrical field of 100 kV/cm (Figure 6(g)). The piezopotentials of the poled PENGs were measured by applying a tapping force of 20 N at 7 Hz. The unpoled sample exhibited a piezopotential of 25.4 V while the samples poled for 5, 10, and 15 h exhibited piezopotentials of 27.7, 30.4, and 34.8 V, respectively (Figure 6(h)). The dipoles of the semiconducting CTO particles and PVDF were randomly oriented before poling; therefore, the obtained piezoelectric potential effect was lower. After poling, the PVDF dipoles were aligned in the amorphous, electroactive, and interfacial areas, and the electrostatic interaction between CTO and PVDF generated an electroactive phase [57]. Figure 6(i) depicts the increase in the piezopotential with time, and the insets show the

unaligned and aligned dipoles before and after poling, respectively. The electrically poled sample possessed prealigned dipoles that enhanced the piezopotential; therefore, the V_{oc} of the 15 h poled sample was 1.3 times higher than that of the unpoled sample.

The CTO2-based PENG was tested under periodic bending/releasing conditions at different bending radii (R_b) (Figure 7(a)). Bending was performed by attaching the PENG device to the sliders of a bending machine, which moved at 0.5 Hz. The bending radius of the PENG was varied from 5 to 1 mm, and the obtained V_{oc} values were 0.72, 1.2, 1.52, 1.64, and 3.76 V, respectively. This indicated that the maximum strain was applied to the PENG at a smaller bending radius, resulting in a higher V_{oc} value. During bending, the CTO particles create local deformations in PVDF [25]. Additionally, the bending frequency varied from 0.1, 0.5, 1, and 1.25 Hz at a bending radius of 1 mm, generating V_{oc} values of 1.64, 3.76, 4.09, and 5.85 V, respectively (Figure 7(b)). The periodic bend/release test was performed for 600 s at 1.25 Hz and a R_b of 1 mm (Figure 7(c)); the CTO2-based PENG exhibited a consistent V_{oc} of 5.9 V, confirming its durability.

The bending cycle of the CTO2-based PENG, with bending based on the slider movement, was initiated in a flat state, which was attained again after release, as shown in Figure 7(d). During bending, strain aligned the dipoles and generated charges on the PENG surface. However, the voltage generated by the bending was relatively low compared

with that generated by tapping. Considering the capability of the CTO2-based PENG to harvest potential from bending movements, the PENGs were attached to a human finger, elbow, and knee to harvest energy from biomechanical bending movements (inset of Figure 7(e)). The finger, elbow, and knee generated maximum voltages of 1.4, 2.8, and 3.3 V at a bending angle of 90°. The piezopotential curves at different bending angles are shown in Figure S6. The available area in the case of the knee was larger, and at 90°, bending imparted sufficient strain to increase the piezopotential, which confirmed the suitability of the CTO2-based PENG for biomechanical applications [53].

Typing on a smartphone or computer keyboard for work or sending messages and emails has become essential for communication. Thus, it was interesting to observe the piezopotential generated by typing activities. A CTO2-based PENG (1.5 cm × 1.5 cm) was attached to the thumb (inset of Figure 8(a)) and, when used for typing on a smartphone, generated 0.7 V (Figure 8(a)). Moreover, another CTO2-based PENG (1 cm × 1 cm) attached to the index finger for computer keyboard typing generated a piezopotential of 0.8 V (Figure 8(a)). The force imparted by the index figure for keyboard typing was 3 N. Thus, the output voltage almost matched the potential generated by tapping (5 N; Figure 6(b)). The output voltage generated during walking was quantified by attaching a CTO2-based PENG (3 cm × 3 cm) to the front of the foot. V_{oc} values were measured at walking speeds of 30, 60, and 90 m/min. Consequently, a force of approximately 8 N was applied to the PENG, which generated piezopotentials of 7.5, 9, and 13 V with an increase in the walking speed. As the walking speed increased, the output voltage also increased because additional pressure was imparted to the front side of the foot while walking at a higher speed.

In addition to power generation applications, piezoelectric materials are gaining increasing attention as tactile sensors in robotic technologies. Thus, for sensor applications, the effect of bending and the force exerted while grasping an object generating a piezopotential can be investigated for the CTO2-based PENG. Thus, a CTO2-PENG (3 cm × 3 cm) was attached to the palm using a glove (Figure 8(c)); in the unfolded state, no force was exerted, and thus, no potential was generated across the PENG. In contrast, in the bent state, a potential of 1.2 V (red box) was generated, and when a mug was grasped, the imparted bending and compressive forces generated 3 V (blue box). The increasing and decreasing piezopotential curves obtained during bending, grasping, and holding are shown in Figure 8(d). The combined force of bending and grasping doubled the potential; when the maximum potential was obtained, a potential balance occurred, and the voltage decreased to zero during the holding state and to a negative value during the released state. The piezoresponse of the PENG during the grasping and holding states indicated its capability to sense dynamic forces. Thus, the various applications demonstrated here confirm that the flexible CTO/PVDF-based PENG can harvest electrical energy based on biomechanical movements.

4. Conclusions

This study fabricated a novel cobalt titanate/PVDF-based PENG using a supersonic cold-spraying technique for harvesting electrical energy via tapping and bending deformations. The CTO particles prepared using a wet chemical process, annealed, and mixed with PVDF to yield an optimal proportion exhibited an output voltage (V_{oc}) of 25.4 V under a tapping force of 20 N and a frequency of 7 Hz. The power density of the device across a load resistance of 0.6 MΩ was 25 μW·cm^{-2}. A poling duration of 15 h further increased the piezopotential to 34.8 V. Moreover, when the PENG was used in a body-attachable form, it demonstrated good sensitivity and energy-harvesting capabilities based on human motions. Thus, the study demonstrates that CTO/PVDF-based flexible PENGs are excellent candidates for next-generation self-powered devices.

Data Availability

The data that support the findings of this study are available from the corresponding authors upon reasonable request.

Conflicts of Interest

The authors declare that they have no conflicts of interest.

Authors' Contributions

Chanwoo Park was responsible for the conceptualization, methodology, and writing—original draft. Bhavana Joshi was responsible for the investigation, formal analysis, and writing—review and editing. Edmund Samuel was responsible for the supervision, visualization, and writing—review and editing. Byeong-yeop Kim was responsible for the methodology, data curation, and investigation. Ali Aldalbahi was responsible for the investigation and validation. Mohamed EL-Newehy was responsible for the supervision and resources. Hae-Seok Lee was responsible for the supervision and resources. Sam S. Yoon was responsible for the supervision, resources, and writing—review and editing. Chanwoo Park, Bhavana Joshi, and Edmund Samuel contributed equally to this work.

Acknowledgments

Supplementary Materials

The details of additional results and tests used in this study are provided in the supplementary materials. Figure S1: XRD patterns of CTO powder and CTO/PVDF samples including CTO1, CTO2, CTO3, and CTO4. Figure S2: the Rietveld refinement plot for synthesized CTO powder.

Figure S3: output voltage of pure PVDF during tapping. Figure S4: illustration of piezopotential generation during mechanical energy harvesting by a PENG device. Figure S5: (a) experimental and theoretical short-circuit current and (b) calculated capacitance of the CTO2-PENG device. Figure S6: PENG performance based on (a) finger, (b) elbow, and (c) knee movements (the inset snapshots show the PENG attached to the body parts and their various bending angles). *(Supplementary Materials)*

References

[1] L. Zhou, L. Zhu, T. Yang et al., "Ultra-stable and durable piezoelectric nanogenerator with all-weather service capability based on N doped 4H-SiC nanohole arrays," *Nano-Micro Letters*, vol. 14, p. 1, 2022.

[2] Z. L. Wang and J. Song, "Piezoelectric nanogenerators based on zinc oxide nanowire arrays," *Science*, vol. 312, no. 5771, pp. 242–246, 2006.

[3] Z. Zhang, Y. Zhang, Y. Zhao et al., "Origin of high piezoelectricity of a bismuth-based organic–inorganic hybrid crystal," *Journal of Materials Chemistry C*, vol. 11, no. 4, pp. 1401–1408, 2023.

[4] G. Jiji, "A retrospect on the role of piezoelectric nanogenerators in the development of the green world," *RSC Advances*, vol. 7, no. 53, pp. 33642–33670, 2017.

[5] S. P. Muduli, S. Veeralingam, and S. Badhulika, "Multilayered piezoelectric nanogenerator based on lead-free Poly(vinylidene fluoride)-(0.67BiFeO3-0.33BaTiO3) electrospun nanofiber mats for fast charging of supercapacitors," *ACS Applied Energy Materials*, vol. 5, no. 3, pp. 2993–3003, 2022.

[6] S. Aaryashree, S. Sahoo, P. Walke, S. K. Nayak, C. S. Rout, and D. J. Late, "Recent developments in self-powered smart chemical sensors for wearable electronics," *Nano Research*, vol. 14, no. 11, pp. 3669–3689, 2021.

[7] R. Yue, S. G. Ramaraj, H. Liu et al., "A review of flexible lead-free piezoelectric energy harvester," *Journal of Alloys and Compounds*, vol. 918, article 165653, 2022.

[8] X. Zheng, Z. Liu, R. Wang, and A. Chen, "Bending-insensitive intrinsically flexible ultraviolet encoding devices based on piezoelectric nanogenerator-supplied liquid crystalline polymer fabrics," *Small*, vol. 18, no. 33, article e2202639, 2022.

[9] B. Joshi, J. Seol, E. Samuel et al., "Supersonically sprayed PVDF and ZnO flowers with built-in nanocuboids for wearable piezoelectric nanogenerators," *Nano Energy*, vol. 112, article 108447, 2023.

[10] W. Deng, Y. Zhou, A. Libanori, G. Chen, W. Yang, and J. Chen, "Piezoelectric nanogenerators for personalized healthcare," *Chemical Society Reviews*, vol. 51, no. 9, pp. 3380–3435, 2022.

[11] S. Sahoo, S. Ratha, C. S. Rout, and S. K. Nayak, "Self-charging supercapacitors for smart electronic devices: a concise review on the recent trends and future sustainability," *Journal of Materials Science*, vol. 57, no. 7, pp. 4399–4440, 2022.

[12] T. Vijayakanth, D. J. Liptrot, E. Gazit, R. Boomishankar, and C. R. Bowen, "Recent advances in organic and organic–inorganic hybrid materials for piezoelectric mechanical energy harvesting," *Advanced Functional Materials*, vol. 32, no. 17, article 2109492, 2022.

[13] Y. Zhang, L. Zhou, C. Liu et al., "Self-powered pacemaker based on all-in-one flexible piezoelectric nanogenerator," *Nano Energy*, vol. 99, article 107420, 2022.

[14] W. Chen, Q. Zheng, Y. A. Lv et al., "Piezoelectric energy harvesting and dissipating behaviors of polymer-based piezoelectric composites for nanogenerators and dampers," *Chemical Engineering Journal*, vol. 465, article 142755, 2023.

[15] C. Zhi, S. Shi, Y. Si, B. Fei, H. Huang, and J. Hu, "Recent progress of wearable piezoelectric pressure sensors based on nanofibers, yarns, and their fabrics via electrospinning," *Advanced Materials Technologies*, vol. 8, no. 5, article 2201161, 2023.

[16] H. Ueda and S. Carr, "Piezoelectricity in polyacrylonitrile," *Polymer Journal*, vol. 16, no. 9, pp. 661–667, 1984.

[17] W. Wang, Y. Zheng, X. Jin et al., "Unexpectedly high piezoelectricity of electrospun polyacrylonitrile nanofiber membranes," *Nano Energy*, vol. 56, pp. 588–594, 2019.

[18] A. Sultana, S. K. Ghosh, V. Sencadas et al., "Human skin interactive self-powered wearable piezoelectric bio-e-skin by electrospun poly-l-lactic acid nanofibers for non-invasive physiological signal monitoring," *Journal of Materials Chemistry B*, vol. 5, no. 35, pp. 7352–7359, 2017.

[19] J. Zhu, L. Jia, and R. Huang, "Electrospinning poly (l-lactic acid) piezoelectric ordered porous nanofibers for strain sensing and energy harvesting," *Journal of Materials Science: Materials in Electronics*, vol. 28, article 12080, 2017.

[20] M. Xu, Y. Wen, F. Niu, Q. Yang, C. Xiong, and Z. Shi, "Flexible piezoelectric generator based on PLLA/ZnO oriented fibers for wearable self-powered sensing," *Composites Part A: Applied Science Manufacturing*, vol. 169, article 107518, 2023.

[21] S. Sahoo, K. Krishnamoorthy, P. Pazhamalai, V. K. Mariappan, S. Manoharan, and S.-J. Kim, "High performance self-charging supercapacitors using a porous PVDF-ionic liquid electrolyte sandwiched between two-dimensional graphene electrodes," *Journal of Materials Chemistry A*, vol. 7, no. 38, pp. 21693–21703, 2019.

[22] B. Mohammadi, A. A. Yousefi, and S. M. Bellah, "Effect of tensile strain rate and elongation on crystalline structure and piezoelectric properties of PVDF thin films," *Polymer Testing*, vol. 26, no. 1, pp. 42–50, 2007.

[23] N. Ismail, M. Essalhi, M. Rahmati, Z. Cui, M. Khayet, and N. Tavajohi, "Experimental and theoretical studies on the formation of pure β-phase polymorphs during fabrication of polyvinylidene fluoride membranes by cyclic carbonate solvents," *Green Chemistry*, vol. 23, no. 5, pp. 2130–2147, 2021.

[24] K. Oflaz and İ. Özaytekin, "Analysis of electrospinning and additive effect on β phase content of electrospun PVDF nanofiber mats for piezoelectric energy harvester nanogenerators," *Smart Materials Structures*, vol. 31, no. 10, article 105022, 2022.

[25] K. Shi, B. Sun, X. Huang, and P. Jiang, "Synergistic effect of graphene nanosheet and $BaTiO_3$ nanoparticles on performance enhancement of electrospun PVDF nanofiber mat for flexible piezoelectric nanogenerators," *Nano Energy*, vol. 52, pp. 153–162, 2018.

[26] P. Martins, A. Lopes, and S. Lanceros-Mendez, "Electroactive phases of poly(vinylidene fluoride): determination, processing and applications," *Progress in Polymer Science*, vol. 39, no. 4, pp. 683–706, 2014.

[27] F. Sun, H. Khassaf, and S. Alpay, "Strain engineering of piezoelectric properties of strontium titanate thin films," *Journal of Materials Science*, vol. 49, no. 17, pp. 5978–5985, 2014.

[28] A. Sasmal, P. S. Devi, and S. Sen, "Influence of various physiochemical parameters of $AFeO_3$ (A= Bi, Er, Ga, La, Sm, Y) fillers on the dielectric, ferroelectric, energy storage, and mechanical

energy harvesting performance of PVDF," *Macromolecular Materials Engineering*, vol. 307, no. 8, article 2200071, 2022.

[29] Y. Zhang, C. Zhang, Y. Feng et al., "Excellent energy storage performance and thermal property of polymer-based composite induced by multifunctional one-dimensional nanofibers oriented in- plane direction," *Nano Energy*, vol. 56, pp. 138–150, 2019.

[30] K. Y. Lee, D. Kim, J. H. Lee, T. Y. Kim, M. K. Gupta, and S. W. Kim, "Unidirectional high-power generation via stress-induced dipole alignment from $ZnSnO_3$ nanocubes/polymer hybrid piezoelectric nanogenerator," *Advanced Functional Materials*, vol. 24, no. 1, pp. 37–43, 2014.

[31] C.-M. Wang, L. Zhao, Y. Liu, R. L. Withers, S. Zhang, and Q. Wang, "The temperature-dependent piezoelectric and electromechanical properties of cobalt-modified sodium bismuth titanate," *Ceramics International*, vol. 42, no. 3, pp. 4268–4273, 2016.

[32] A. Mondal, M. Faraz, and N. Khare, "Magnetically tunable enhanced performance of $CoFe_2O_4$–PVDF nanocomposite film-based piezoelectric nanogenerator," *Applied Physics Letters*, vol. 121, no. 10, 2022.

[33] S. Sinha-Ray, M. W. Lee, S. Sinha-Ray et al., "Supersonic nanoblowing: a new ultra-stiff phase of nylon 6 in 20–50 nm confinement," *Journal of Materials Chemistry C*, vol. 1, no. 21, p. 3491, 2013.

[34] H. S. Jo, S. An, C.-W. Park, D.-Y. Woo, A. L. Yarin, and S. S. Yoon, "Wearable, stretchable, transparent all-in-one soft sensor formed from supersonically sprayed silver nanowires," *ACS Applied Materials Interfaces*, vol. 11, no. 43, pp. 40232–40242, 2019.

[35] S. An, B. Joshi, A. L. Yarin, M. T. Swihart, and S. S. Yoon, "Supersonic cold spraying for energy and environmental applications: one-step scalable coating technology for advanced micro-and nanotextured materials," *Advanced Materials Technologies*, vol. 32, article 1905028, 2020.

[36] J.-G. Lee, B. N. Joshi, J.-H. Lee et al., "Stable high-capacity lithium ion battery anodes produced by supersonic spray deposition of hematite nanoparticles and self-healing reduced graphene oxide," *Electrochimica Acta*, vol. 228, pp. 604–610, 2017.

[37] T. Kim, C. Park, E. P. Samuel et al., "Supersonically sprayed washable, wearable, stretchable, hydrophobic, and antibacterial rGO/AgNW fabric for multifunctional sensors and supercapacitors," *ACS Applied Materials Interfaces*, vol. 13, no. 8, pp. 10013–10025, 2021.

[38] E. Samuel, T. G. Kim, C. W. Park, B. Joshi, M. T. Swihart, and S. S. Yoon, "Supersonically sprayed Zn_2SnO_4/SnO_2/CNT nanocomposites for high-performance supercapacitor electrodes," *ACS Sustainable Chemistry Engineering*, vol. 7, no. 16, pp. 14031–14040, 2019.

[39] S. De, D. Asthana, C. Thirmal et al., "A folded π-system with supramolecularly oriented dipoles: single-component piezoelectric relaxor with NLO activity," *Chemical Science*, vol. 14, no. 10, pp. 2547–2552, 2023.

[40] K. Shi, X. Huang, B. Sun, Z. Wu, J. He, and P. Jiang, "Cellulose/ $BaTiO_3$ aerogel paper based flexible piezoelectric nanogenerators and the electric coupling with triboelectricity," *Nano Energy*, vol. 57, pp. 450–458, 2019.

[41] H. Guo, Q. Wu, H. Sun, X. Liu, and H. Sui, "Organic phosphonic acid-modified $BaTiO_3$/P(VDF-TrFE) composite with high output in both voltage and power for flexible piezoelectric nanogenerators," *Materials Today Energy*, vol. 17, article 100489, 2020.

[42] B. Zhao, Z. Chen, Z. Cheng et al., "Piezoelectric nanogenerators based on electrospun PVDF-coated mats composed of multilayer polymer-coated $BaTiO_3$ nanowires," *ACS Applied Nano Materials*, vol. 5, no. 6, pp. 8417–8428, 2022.

[43] S. Patel and R. Kumar, "Synthesis and characterization of magnesium ion conductivity in PVDF based nanocomposite polymer electrolytes disperse with MgO," *Journal of Alloys Compounds*, vol. 789, p. 6, 2019.

[44] A. Bouhamed, Q. Binyu, B. Böhm et al., "A hybrid piezoelectric composite flexible film based on PVDF-HFP for boosting power generation," *Composites Science and Technology*, vol. 208, article 108769, 2021.

[45] M. S. Ramasamy, A. Rahaman, and B. Kim, "Influence of oleylamine–functionalized boron nitride nanosheets on the crystalline phases, mechanical and piezoelectric properties of electrospun PVDF nanofibers," *Composites Science and Technology*, vol. 203, article 108570, 2021.

[46] E. Soergel, "Piezoresponse force microscopy (PFM)," *Journal of Physics D: Applied Physics*, vol. 44, no. 46, article 464003, 2011.

[47] S. M. Neumayer, S. Saremi, L. W. Martin et al., "Piezoresponse amplitude and phase quantified for electromechanical characterization," *Journal of Applied Physics*, vol. 128, no. 17, article 171105, 2020.

[48] T. D. Usher, K. R. Cousins, R. Zhang, and S. Ducharme, "The promise of piezoelectric polymers," *Polymer International*, vol. 67, no. 7, pp. 790–798, 2018.

[49] B. Bera and M. D. Sarkar, "Piezoelectricity in PVDF and PVDF based piezoelectric nanogenerator: a concept," *IOSR Journal of Applied Physics*, vol. 9, no. 3, pp. 95–99, 2017.

[50] S. Paria, S. K. Karan, R. Bera et al., "A facile approach to develop a highly stretchable PVC/$ZnSnO_3$ piezoelectric nanogenerator with high output power generation for powering portable electronic devices," *Industrial Engineering Chemistry Research*, vol. 55, no. 40, pp. 10671–10680, 2016.

[51] R. Sillars, "The properties of a dielectric containing semiconducting particles of various shapes," *Journal of the Institution of Electrical Engineers*, vol. 80, no. 484, pp. 378–394, 1937.

[52] M. Arous, H. Hammami, M. Lagache, and A. Kallel, "Interfacial polarization in piezoelectric fibre-polymer composites," *Journal of Non-Crystalline Solids*, vol. 353, no. 47-51, pp. 4428–4431, 2007.

[53] J. Yoo, S. Cho, W. Kim et al., "Effects of mechanical deformation on energy conversion efficiency of piezoelectric nanogenerators," *Nanotechnology*, vol. 26, no. 27, article 275402, 2015.

[54] G. Zhang, Q. Liao, M. Ma et al., "A rationally designed output current measurement procedure and comprehensive understanding of the output characteristics for piezoelectric nanogenerators," *Nano Energy*, vol. 30, pp. 180–186, 2016.

[55] M. Sahu, S. Hajra, K. Lee, P. Deepti, K. Mistewicz, and H. J. Kim, "Piezoelectric nanogenerator based on lead-free flexible PVDF-barium titanate composite films for driving low power electronics," *Crystals*, vol. 11, no. 2, p. 85, 2021.

[56] S. Panda, S. Hajra, H. Jeong et al., "Biocompatible $CaTiO_3$-PVDF composite-based piezoelectric nanogenerator for exercise evaluation and energy harvesting," *Nano Energy*, vol. 102, article 107682, 2022.

[57] G. Martínez-Ayuso, M. I. Friswell, H. H. Khodaparast, J. I. Roscow, and C. R. Bowen, "Electric field distribution in porous piezoelectric materials during polarization," *Acta Materialia*, vol. 173, pp. 332–341, 2019.